INTERNATIONAL JOURNAL OF HYDROGEN ENERGY 45 (2020) 14867–14879

Available online at www.sciencedirect.com

ScienceDirect

journal homepage: www.elsevier.com/locate/he

$Mn_xCo_{3-x}O_4$ spinel oxides as efficient oxygen evolution reaction catalysts in alkaline media

K. Lankauf [a,*], K. Cysewska [a], J. Karczewski [b], A. Mielewczyk-Gryń [b], K. Górnicka [b], G. Cempura [c], M. Chen [d], P. Jasiński [a], S. Molin [a]

[a] Faculty of Electronics, Telecommunications and Informatics, Gdańsk University of Technology, ul. G. Narutowicza 11/12, 80-233 Gdańsk, Poland

[b] Faculty of Applied Physics and Mathematics, Gdańsk University of Technology, ul. G. Narutowicza 11/12, 80-233 Gdańsk, Poland

[c] International Centre of Electron Microscopy for Materials Science, AGH University of Science and Technology, al. A. Mickiewicza 30, 30-059 Kraków, Poland

[d] Department of Energy Conversion and Storage, Technical University of Denmark, Frederiksborgvej 399, 4000, Roskilde, Denmark

HIGHLIGHTS

- $Mn_xCo_{3-x}O_4$ spinel oxides were synthesised via a soft chemistry method.
- The effect of Mn addition on structural and physicochemical properties was investigated.
- Synthesised oxides powders were examined as OER catalysts in alkaline medium.
- Synergistic effect of dual phase $MnCo_2O_4$ improves the OER catalytic activity.

GRAPHICAL ABSTRACT

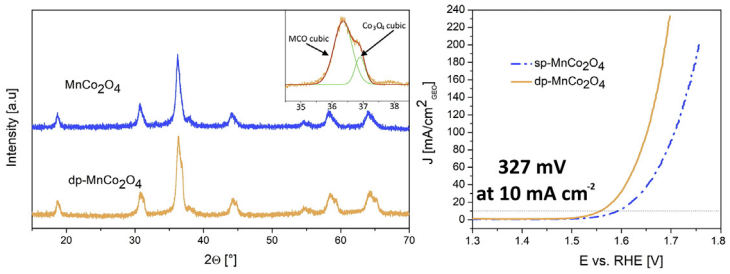

ARTICLE INFO

Article history:
Received 10 February 2020
Received in revised form
20 March 2020
Accepted 26 March 2020
Available online 23 April 2020

Keywords:
Manganese cobaltite
Oxygen evolution reaction

ABSTRACT

The design of efficient electrocatalysts for oxygen evolution reaction (OER) is an essential task in developing sustainable water splitting technology for the production of hydrogen. In this work, manganese cobalt spinel oxides with a general formula of $Mn_xCo_{3-x}O_4$ ($x = 0, 0.5, 1, 1.5, 2$) were synthesised via a soft chemistry method. Non-equilibrium mixed powder compositions were produced, resulting in high electrocatalytic activity. The oxygen evolution reaction was evaluated in an alkaline medium (1 M KOH). It was shown that the addition of Mn (up to $x \leq 1$) to the cubic Co_3O_4 phase results in an increase of the electrocatalytic performance. The lowest overpotential was obtained for the composition designated as $MnCo_2O_4$, which exhibited a dual-phase structure (~30% Co_3O_4 + 70% $Mn_{1.4}Co_{1.6}O_4$): the benchmark current density of 10 mA cm^{-2} was achieved at the relatively low overpotential of 327 mV. The corresponding Tafel slope was determined to be ~79 mV dec^{-1}.

* Corresponding author.
E-mail address: krystian.lankauf@pg.edu.pl (K. Lankauf).

https://doi.org/10.1016/j.ijhydene.2020.03.188

Spinel oxides
Water splitting

Stabilities of the electrodes were tested for 25 h, showing degradation of the $MnCo_2O_4$ powder, but no degradation, or even a slight activation for other spinels.

Introduction

Among different hydrogen production methods, water electrolysis seems to be a viable process to provide clean hydrogen [1,2], especially when coupled with renewable electricity production. The key point impeding the electrolysis process is the sluggish oxygen evolution reaction (OER) kinetics of the multi-electron charge transfer reaction resulting in high reaction overpotentials [3,4]. For this reason, effective electrocatalysts may be applied to accelerate the reaction and reduce the overpotential. The most active catalysts for water splitting reactions, hydrogen and oxygen evolution, are based on precious elements: Pt and IrO_2, respectively. Their low abundance in the Earth's crust coupled with high costs significantly limits those elements' application for water splitting electrodes.

Recently, researchers have shown an increased interest in 3d transition-metals OER electrocatalysts, especially in oxides with perovskite [5–7] and spinel structures [8–14], layered double hydroxides (LDH) [15–17] and carbides [18–20]. For example, She et al. reported an $Sr(Co_{0.8}Fe_{0.2})_{0.7}B_{0.3}O_{3-\delta}$ (SCFB-0.3) perovskite realising ultrafast oxygen evolution with overpotential (η) at 10 mA cm^{-2} of 240 mV in 1.0 M KOH aqueous electrolyte [21]. Cubic structure Co_3O_4 spinel nanoparticles with average diameters of 5.9 nm were synthesised by Esswein et al. and demonstrated η of 328 mV at 10 mA cm^{-2} in 1.0 M KOH [22]. One of the promising spinel group materials is mixed-valent $Mn_xCo_{3-x}O_4$ due to the possibility of tuning the cation distribution by changing the synthesis parameters and composition. Mn-Co spinels have interesting flexible properties and have been reported both for oxygen reduction [23] and evolution processes. Han et al. fabricated mixed phases of Co- and Mn-based oxides which for OER demonstrated η of 450 mV at 10 mA cm^{-2} in 1.0 M KOH with a low Tafel slope of 35.8 mV dec^{-1} [24]. The hybrid nanostructure of manganese cobaltite/nitrogen-doped multi-walled carbon nanotubes ($Mn_xCo_{3-x}O_4$@NCNTs) was proposed by Zhao et al. and exhibited an overpotential of 470 mV at 10 mA cm^{-2} in 0.1 M KOH [25].

The physicochemical properties of the spinels can be tailored by manipulating different cations and also by altering their preparation methods. Spinels can be synthesised by different approaches, including physical and preferably chemical processes: hard-template [26], wet-chemical [27], hydrothermal [28,29], solvothermal [30], spray pyrolysis [31], co-precipitation [32], and sol-gel [22,33–35]. Depending on the thermal history, the cation distribution may vary resulting in data scattering and uncertainties.

In this work, series of $Mn_xCo_{3-x}O_4$ (x = 0, 0.5, 1, 1.5, 2) spinels were prepared by an ethylenediamine tetra acetic acid - citric acid - ethylene glycol (EDTA-CA-EG) process, and were tested as OER catalysts in an alkaline media (1M KOH). The purpose of this study was to explore the relationship between the Mn content in the Co-based spinel structure and its electrocatalytic activity.

Experimental section

Powder synthesis

The spinel powders evaluated in this work were synthesised via a sol-gel EDTA-citric acid-ethylene glycol method. The initial compounds with thermogravimetrically standardised cation content: $Mn(NO_3)_2 \cdot 4H_2O$ and $Co(NO_3)_2 \cdot 6H_2O$ (analytical grade) were dissolved in deionised water and added to a mixture of CA and EDTA. The solution was stirred for 10 min on a magnetic stirrer at room temperature. In order to avoid the risk of citrate protonation or metal hydroxide precipitation, the pH of the solution was sustained at a level of 6 by the addition of ammonia solution (25% solution, POCH, Poland). Ethylene glycol (EG, Aldrich) was added and the temperature of the solution was increased up to 80 °C in order to initiate the transesterification reaction, and was kept overnight until all solvents evaporated, leaving a semi-solid gel. The specific molar ratio of the reagents was maintained, i.e. TMI:CA:EDTA:EG = 1:2:1:2 (*TMI -Total Metal Ions*). The obtained gel was heated in a muffle furnace first at 130 °C to ensure the evaporation of residual solvents. Subsequently, the gel was pre-calcined at 400 °C, ground in an agate mortar and calcined at a final temperature of 600 °C. The calcined powders were ball-milled in isopropanol with yttria-stabilised zirconia (YSZ) spherical grinding media (φ3 mm) for the purpose of agglomerate defragmentation with the intention of improving electrocatalytic performance [4]. After milling, powders were dried in a laboratory drier at 100 °C in the air.

Powder analysis

Crystalline phases were identified by powder X-ray diffraction (pXRD), conducted at room temperature on a Bruker D2 Phaser diffractometer with CuK_α radiation (λ = 1.5404 Å) and a LynxEye XE-T detector. The results were analysed by Rietveld refinement using the Fullprof software package [36]. The.cif files required to perform the analyses were downloaded from the Crystallography Open Database [37,38]. Calculation of MnOx-CoOx phase diagram in air was done utilising the Thermo-Calc software [39] with the thermodynamic description of Co-Mn-O developed by Weiland [40]. FEI Quanta 250 FEG, and Thermo Fisher Phenom XL scanning Electron

Microscopes (SEM), and a C_s-corrected Titan Cubed G2 60-300 (FEI) Scanning Transmission Electron Microscope (S/TEM) were used to investigate the morphologies and chemical composition (using the ChemiSTEM EDX system based on 4 windowless Silicon Drift Detectors (Super X) of the as-prepared powders). The powders for TEM investigations were prepared traditionally: a drop of a water suspension containing the powder was placed onto a copper grid followed by vacuum drying. The specific surface areas were determined by means of the 10-point Brunauer–Emmett–Teller (BET) method: the N_2 adsorption isotherms were measured by a Quantachrome Instruments Autosorb iQ analyser. Assuming a spherical geometry, the mean sizes of the powders' particles were calculated by the following equation:

$$d = \frac{6000}{A_{BET}\rho} \quad (1)$$

where d is particle diameter, A_{BET} is the BET specific surface area, and ρ is the theoretical density calculated based on data obtained from Rietveld.

Preparation of electrodes for OER

Highly porous Ni foam (1.6 mm thick, 110 ppi, Shanghai Tankii Alloy Material Co. Ltd., China) was cut into smaller samples in the shape of a square with a working (active) area of 1 cm^2 with an additional holding/electrical connection part. Before the deposition of the catalyst inks, the nickel was cleaned in deionised water and, subsequently in acetone for 5 min in an ultrasonic bath. Then, the Ni foam was dried in a laboratory drier at 100 °C in the air for at least 1 h. The electrocatalyst inks were prepared by mixing 100 mg of the prepared spinel powders, 100 mg Timcal Super C45 Conductive Carbon Black (Imerys, Belgium), and 6 ml of Ethyl Alcohol Absolut 99.8% Pure (POCH, Poland). The prepared mixture was ball-milled for 24 h. Afterwards, the milling balls were rinsed with 4 ml of ethanol and the powder drying step was skipped to avoid re-agglomeration. After the milling step, 1 ml of 5% Nafion 117 solution was added to the mixture as an ink dispersant and a catalyst binder [41,42]. At the end, the ink was sonicated in a water bath for 30 min to obtain a homogeneous colloid. The catalyst ink was pipetted onto the cleaned Ni foam to achieve a mass loading of 1.3 mg, and dried overnight in ambient conditions.

For comparison, reference IrO_2 (PK Catalyst, FuelCellStore, USA) electrodes were prepared in the same manner as the other ones.

Electrochemical tests

The electrochemical measurements were performed in a three-electrode glass cell system in 1.0 M KOH aqueous solution. A HydroFlex reversible hydrogen reference electrode (RHE) (Gaskatel, Germany), a Pt sheet, and a coated Ni foam were used as the reference (RE), counter (CE), and working (WE) electrodes, respectively. The electrochemical tests were performed using an Ametek VersaSTAT 4 potentiostat/galvanostat/impedance meter. All measurements were carried out at 25 °C, maintained by a Julabo F12 thermostat. Before each measurement, the electrolyte was purged with high purity argon for 20 min. After purging, the working electrode was cycled between 1.1 V and 1.6 V vs. RHE at a scan rate of 100 mV s^{-1} for 40 (example of activation procedure is shown Fig. S1). This treatment reduces the activity of the electrodes but allows to achieve stable performance and reproducible results. Cycling voltammetry (CV) scans were performed in the non-faradaic potential region from 1.15 V to 1.25 V (vs. RHE) at scan rates of 10, 20, 40, 60, 80, 100 mV s^{-1} in order to estimate the double-layer capacitance (C_{dl}). Then, the values of C_{dl} were used to assess the electrochemical active surface area (ECSA) of the material [21,43]. To obtain the surface area values from the specific capacitances, a reference capacitance value of 40 μF cm^{-2} was assumed [44]. Linear sweep voltammetry (LSV) data were collected from 1.1 to 2.0 V (vs. RHE) at a scan rate of 5 mV s^{-1}. Electrochemical impedance spectroscopy (EIS) measurements were carried out to investigate the electrical properties of the materials, i.e. the charge transfer resistance R_{ct}. Measurements were performed in the frequency range from 10 kHz to 0.1 Hz at 1.7 V vs. RHE with an amplitude of 10 mV. For the quantitative analysis, a fitting to a modified Randles equivalent circuit was carried out using the Zview software. To evaluate the temporal stability of the electrodes, chronopotentiometry was performed at 10 mA cm^{-2} for 25 h.

All potential values were iR-corrected to remove the effect of solution resistance according to the equation $E_{iR\text{-}corrected} = E_{applied} - iR_{un}$, where i is the current, and R_{un} is an uncompensated ohmic electrolyte resistance. The overpotential (η) for the oxygen evolution reaction was calculated by the following equation: $\eta = E\,(10\ mA \cdot cm^{-2}) - 1.23$ V (vs. RHE). The current density was normalised by the geometrical surface area of the working electrode (1 cm^2). The catalyst mass activity at specific overpotential values was calculated by current normalisation by the catalyst oxide loading (~1.3 mg).

Results and discussion

Catalyst characterisation

$Mn_xCo_{3-x}O_4$ (x = 0, 0.5, 1, 1.5, 2) spinel powders were synthesised by a EDTA-CA-EG process. Utilisation of the soft-chemistry based synthesis method leads to powders with a small particle size and high specific surface area, which is beneficial for the catalysis. The powders' morphologies, observed by SEM, are presented in Fig. 1. Submicron particles were obtained for all compositions. It was observed that the introduction of Mn into the Co-based spinel results in finer particles (enlarged images are shown in Fig. S2). This observation is confirmed by specific surface area (SSA-BET) measurements. The specific surface area of the powders increases on the addition of Mn with x = 0.5, and then decreases for a higher Mn content. The $Mn_{0.5}Co_{2.5}O_4$ powder has the highest specific area of 32.9 m^2 g^{-1}. Interestingly, for the Mn-rich Mn_2CoO_4 composition, the SSA is similar to the pure Co_3O_4 spinel, indicating a complex influence of the Mn on the particle size. Based on the SSA, particle sizes were calculated, and the values are presented in Table 1. The obtained values are consistent with the SEM images, denoting submicrometric grains, with particles in the 30–100 nm range.

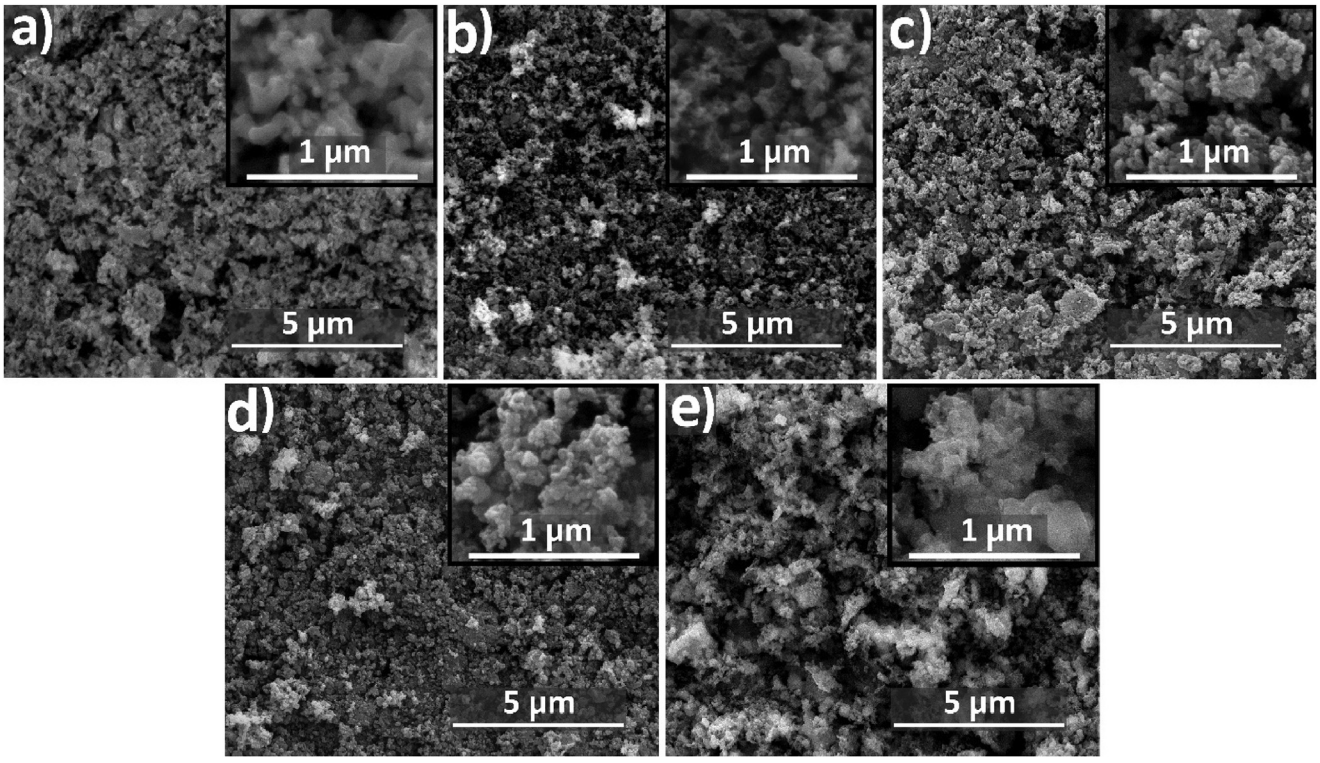

Fig. 1 – SEM images of synthesised $Mn_xCo_{3-x}O_4$ powders (a) x = 0, (b) x = 0.5, (c) x = 1, (d) x = 1.5 and x = 2.

Table 1 – Properties of the prepared $MnxCo_3$-xO_4 powders (EDS and BET analyses results).

Material	Theoretical ratio Mn:Co	EDS analysis results			Corresponding composition	Surface area [$m^2\ g^{-1}$]	Particle diameter [nm]
		Mn [at. %]	Co [at. %]	Mn:Co			
Co_3O_4	–	–	100	–	Co_3O_4	9.6	103
$Mn_{0.5}Co_{2.5}O_4$	0.2	18.2	81.8	0.22	$Mn_{0.55}Co_{2.45}O_4$	32.9	30
$MnCo_2O_4$	0.5	32.3	67.7	0.48	$Mn_{0.97}Co_{2.03}O_4$	17.6	59
$Mn_{1.5}Co_{1.5}O_4$	1	46.9	53.1	0.89	$Mn_{1.41}Co_{1.59}O_4$	20.0	56
Mn_2CoO_4	2	65.4	34.6	1.88	$Mn_{1.96}Co_{1.04}O_4$	9.5	124

In order to evaluate the chemical compositions of the synthesised powders, EDS analyses were performed (quantitative results are included in Table 1 and the obtained EDS spectra are shown in Fig. S3). The Mn:Co ratios in the synthesised powders were close to the desired ones.

In order to determine the crystallographic structure and phase purity of the synthesised $Mn_xCo_{3-x}O_4$ powders, X-ray diffraction (pXRD) characterisation was performed, followed by Rietveld refinement of the unit cell parameters. The pXRD patterns are shown in Fig. 2, and the obtained results are summarised in Table 2. For the Mn_2CoO_4 compound, all of the diffraction peaks correspond to the tetragonal crystal structure (space group I41/amd), whereas all reflections for the Co_3O_4 and $Mn_{0.5}Co_{2.5}O_4$ compounds are indexed in the cubic spinel phase (space group Fd3m). In the case of $Mn_{0.5}Co_{2.5}O_4$, the peaks are broader, indicating a smaller crystallite size. Similar phenomena was observed by Zhang et al. for $MnCo_2O_4$ [45].

The powder designated as $MnCo_2O_4$, which was expected to crystallise in a single cubic phase, shows the presence of two phases. Analysis of the peaks reveals the formation of two phases with similar structure (with the same space group). The phases differ by cation composition and thus a shift of the peaks is visible in the spectra. One of the phases (based on lattice constant value) is similar to the pure Co_3O_4 phase, and the other must contain the Mn and Co. The elemental content, i.e. the Mn:Co ratio in the powder, has been confirmed by EDS, as presented in Table 1. For this particular cation ratio, a single cubic phase is expected as presented in the literature [46–48]. By rough analysis of the peaks' intensity, the amount of Co_3O_4 phase in the mixed powder is estimated to be ~30 vol%. Assuming that some of the Co atoms were consumed to form the pure Co_3O_4 phase, the rough calculation of the stoichiometry of the second phase is $Mn_{1.4}Co_{1.6}O_4$.

In order to verify the result, the synthesis of the spinel was repeated, and the same result was obtained. In order to exclude possible influence of a too-short annealing step, an additional thermal annealing step was carried out. The powders were subjected to a second heat treatment of 600 °C for 2 h, yielding the same mixed structure (Fig. S4). Therefore the

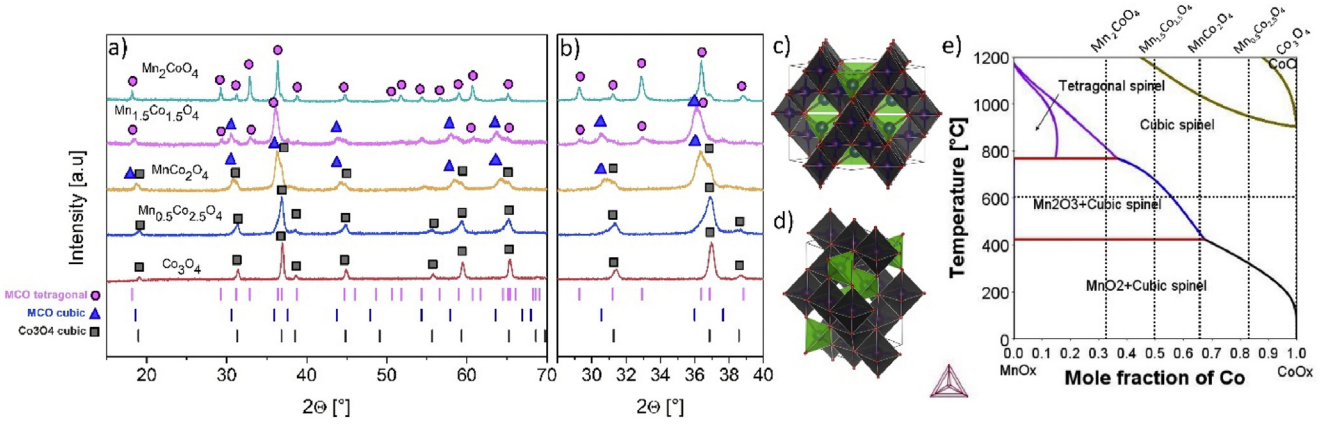

Fig. 2 – XRD patterns of synthesised $Mn_xCo_{3-x}O_4$ powders (a) and partially enlarged patterns (b), cubic (c) and tetragonal (d) spinel unit cells, e) calculated MnOx-CoOx phase diagram in air based on the thermodynamic description in the literature [40].

Table 2 – Rietveld analysis results. Cubic/tetragonal phase contribution (weight fraction(%)) and unit cell parameters.

Material	Cubic phase (Fd3m)	Tetragonal phase (I41/amd)	a_C [Å]	$a_T = b_T$ [Å]	c_T [Å]
Co_3O_4	100%	–	8.086(1)	–	–
$Mn_{0.5}Co_{2.5}O_4$	100%	–	8.1246(3)	–	–
$MnCo_2O_4$	100%	–	8.1926(4) ($Mn_{1.4}Co_{1.6}O_4$)	–	–
	~70% $Mn_{1.4}Co_{1.6}O_4$ ~30?% Co_3O_4		8.0812(4) (Co_3O_4)		
$Mn_{1.5}Co_{1.5}O_4$	85%	15%	8.2669(5)	5.7426(4)	9.2583(5)
Mn_2CoO_4	–	100%	–	5.7270(2)	9.2797(4)

structure of the spinel is reproducible. For the spinel initially designated as $MnCo_2O_4$, to highlight the phase composition of the powder, the name "dual-phase $MnCo_2O_4$" spinel will be used in the remainder of the work.

We postulate, that the mixed-phase composition of the dual-phase $MnCo_2O_4$ spinel (Co_3O_4+$Mn_{1.4}Co_{1.6}O_4$) results from the use of a modified EDTA-CA-EG powder synthesis method. When utilising a pure EDTA-CA synthesis method (with no EG), only a single cubic spinel was produced (results included in Fig. S5, full results will be reported elsewhere). Interestingly, the single phase $MnCo_2O_4$ powder revealed much lower performance towards OER than the dual phase powder. Apparently, due to the different binding/chelating powers of the acids/EG, different powders were produced.

The powder with the intended stoichiometry of $Mn_{1.5}Co_{1.5}O_4$ consisted of two phases: cubic (85%) and tetragonal (15%), while the Mn_2CoO_4 was entirely tetragonal. These powders have structures according to the reported ones.

Calculation of MnO_x – CoO_x phase diagram in the air was performed in order to compare structures of prepared powders with theoretical data. According to Fig. 2e, Mn has four different oxides, from low to high temperature, MnO_2, Mn_2O_3, tetragonal Mn_3O_4 spinel and cubic Mn_3O_4 spinel, while Co has two stable oxides, cubic Co_3O_4 spinel and CoO. Tetragonal Mn_3O_4 spinel has limited Co solubility, while the two cubic spinels are mutually soluble. In general, the phase diagram does not predict the existence of a single phase only material at room temperatures (other than pure Co_3O_4 spinel). For the mixed Mn-Co compositions at room temperature, a mixed phase system composed of tetragonal MnO_2-cubic Mn-Co spinel are predicted.

For comparison, Brylewski et al. have synthesised and analysed $Mn_{1+x}Co_{2-x}O_4$ with x = 0, 0.25, 0.5, 0.75, 1.0, and 1.5 by EDTA-gel processes [49]. In their work, the $Mn_{1.5}Co_{1.5}O_4$ powders were composed of mostly the tetragonal phase (~68%) and the remaining, cubic phase (~32%). For the $MnCo_2O_4$ and $Mn_{1.25}Co_{1.75}O_4$, only a cubic phase was detected. The lattice constant for the latter spinel was reported to be 8.31 Å, while for the $Mn_{1.15}Co_{1.85}O_4$ spinel reported in this work, a = 8.19 Å. Talic et al. performed the characterisation on sintered pellets, which can give different results to powder analysis [50]. In other work, Bobruk et al. have analysed $Mn_{1.2}Co_{1.8}O_4$ powders synthesised by different soft-chemistry methods [51]. The cation composition is thus quite similar to the one obtained for the Mn-containing phase in the $MnCo_2O_4$ designated sample. For XRD, the powders were calcined at 800 °C. Interestingly, depending on the precipitation agent used, either single or double phase materials were obtained. This highlights the complex nature of the spinels, and the possible effects on their structure. For the case where the pure cubic spinel phase was obtained (using EDTA as the precipitation/chelating agent), the lattice parameter was ~8.20 Å, so comparable with the one obtained in our study.

In order to further characterise the catalyst with the nominal composition of $MnCo_2O_4$, transmission electron microscopy (TEM) analyses were performed. Fig. 3 (and Fig. S6)

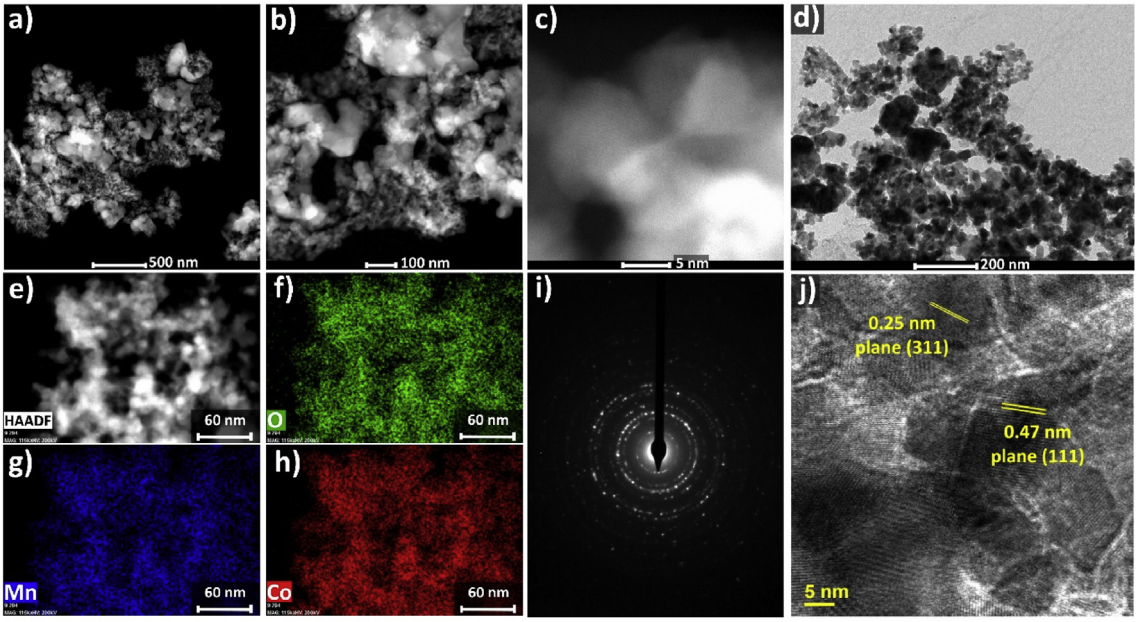

Fig. 3 – HAADF-(S)TEM images (a–d) and corresponding SAED (i) and HRTEM (j) patterns of the dual-phase $MnCo_2O_4$ powder. TEM-EDS elemental maps (e–h) of oxygen (f), manganese (g), and cobalt (h).

presents high-angle annular dark-field (HAADF) images, a TEM-EDS elemental analysis, and selected area electron diffraction (SAED) patterns. From the TEM images, it can be observed (Fig. 3a and b) that the synthesised material consists of nanocrystals in two size ranges i.e. < 50 nm and >100 nm. EDS mapping shows that Co and Mn are mutually well dispersed in the powder volume in the case of the small particles (Fig. 3e). Additionally, the HRTEM image (Fig. 3j) reveals the lattice fringes with an inter-planar spacing of 0.25 nm, corresponding to the <311> plane, and 0.47 nm, corresponding to the <111> plane of the $Mn_{1.4}Co_{1.6}O_4$ phase. The SAED patterns confirm the well-defined polycrystalline structure of $MnCo_2O_4$. TEM/EDS analysis of the larger particles confirms that the larger particles are composed of mostly pure Co oxide, as previously discussed, based on the XRD results. The smaller particles contain more Co than Mn. The $MnCo_2O_4$ powders thus consist of very fine (<30 nm diameter) $Mn_{1.4}Co_{1.6}O_4$ particles and larger (>100 nm diameter) Co_3O_4 particles.

For the electrochemical study, the produced spinel oxides were deposited on highly porous nickel foam substrates (porosity > 95%). For the determination of the coating quality, i.e. the homogeneity of catalyst distribution, scanning

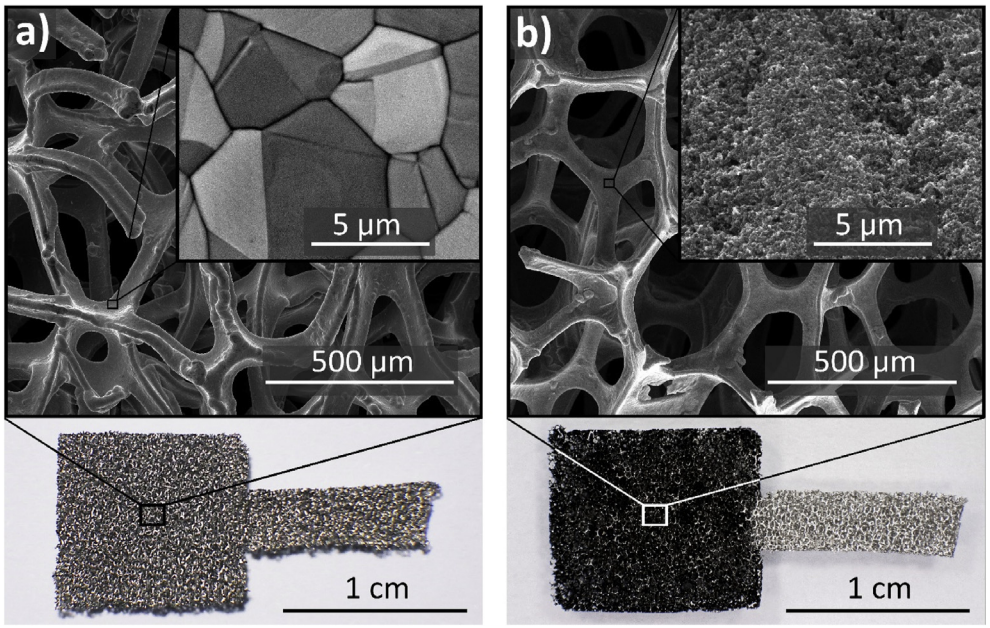

Fig. 4 – Electrodes used in electrochemical tests: (a) bare Ni foam, (b) Ni foam coated with dual-phase $MnCo_2O_4$ catalyst.

Table 3 – Comparison of OER activity data for examined catalysts.

Electrode material	η at J = 10 mA cm^{-2} [mV]	Tafel slope [mV dec^{-1}]	R_{ct} [Ω cm^2]	$ECSA_{(abs)}$ [cm^2]	$ECSA_{(g)}$ [m^2 g^{-1}]
Ni foam	388	73.1	2.23	43	3.3
Co_3O_4	368	75.5	0.98	75	5.8
$Mn_{0.5}Co_{2.5}O_4$	345	74.3	0.78	78	6.0
dual-phase $MnCo_2O_4$	327	78.9	0.69	143	11.0
$Mn_{1.5}Co_{1.5}O_4$	371	79.9	1.06	85	6.5
Mn_2CoO_4	399	78.9	1.52	53	4.1
IrO_2	289	82.2	1.29	115	8.8

electron and visible light microscopy analyses were performed. Images of the Ni foam before the catalyst deposition and after the catalyst deposition are presented in Fig. 4. The nickel foam had visible grains within a size range of 5–20 μm. The prepared catalyst ink was distributed evenly over the active area of the porous foam, the surface coverage being very uniform. The total amount of the catalyst spinel powder was ~1.3 mg. SEM images confirm the uniform microstructure of the catalyst, with no agglomerates visible.

Evaluation of electrocatalytic activity for OER

The electrocatalytic OER performance of the $Mn_xCo_{3-x}O_4$ spinels was investigated in 1.0 M KOH solution. For comparison, pure Ni foam and Ni foam coated with commercial IrO_2 catalyst were also examined. Based on the LSV polarisation curves presented in Fig. 5a, it can be observed that all of the spinel catalysts outperformed the pure Ni foam electrode. Among the spinels, the lowest performance was determined for the tetragonal Mn_2CoO_4, whereas the best performance was found for the dual-phase $MnCo_2O_4$ material (Co_3O_4/$Mn_{1.4}Co_{1.6}O_4$).

The electrode overpotential determined at 10 mA cm^{-2}, Tafel slope, R_{ct}, and ECSA are the most common parameters determined and used to assess the catalytic performance of an electrode towards OER. These values obtained for the studied materials are summarised in Table 3. The results indicate that the lowest overpotential (η) at 10 mA cm^{-2} of 289 mV was exhibited by IrO_2 but its performance weakened at higher overpotentials compared to the other synthesised spinels. Pure tetragonal Mn_2CoO_4 spinel showed very low catalytic activity, the overpotential was even slightly higher than the overpotential obtained for the pure nickel. Therefore, this phase can be considered inactive towards OER. The activity obtained for the pure Co_3O_4 spinel was slightly better in comparison to the nickel foam. For the $Mn_{1.5}Co_{1.5}O_4$, which was a mixture of the tetragonal and cubic phases, the performance was comparable to the Co_3O_4 catalyst.

The dual-phase $MnCo_2O_4$ exhibited the lowest η of 327 mV. Since it was a mixture of Co_3O_4 (~30 vol%) and $Mn_{1.4}Co_{1.6}O_4$ (~70 vol%), with the former being only a mediocre catalyst (LSV curves obtained for dp-$MnCo_2O_4$ and sp-$MnCo_2O_4$ are compared in Fig. S7), either the latter has very high activity or there exist some synergistic interaction between the two phases. Also, as based on the TEM analyses, the Mn-Co phase in the mixed catalyst had a much finer structure, preferable for the surface-driven OER. In any case, the dual-phase spinel designated as $MnCo_2O_4$ is an interesting alternative to the state-of-the-art IrO_2 in the role of OER catalyst.

From Fig. 5b, it can be seen that the Tafel slopes for all measured spinels are very similar (70–80 mV dec^{-1}) and are slightly lower compared to IrO_2. The results indicate that the

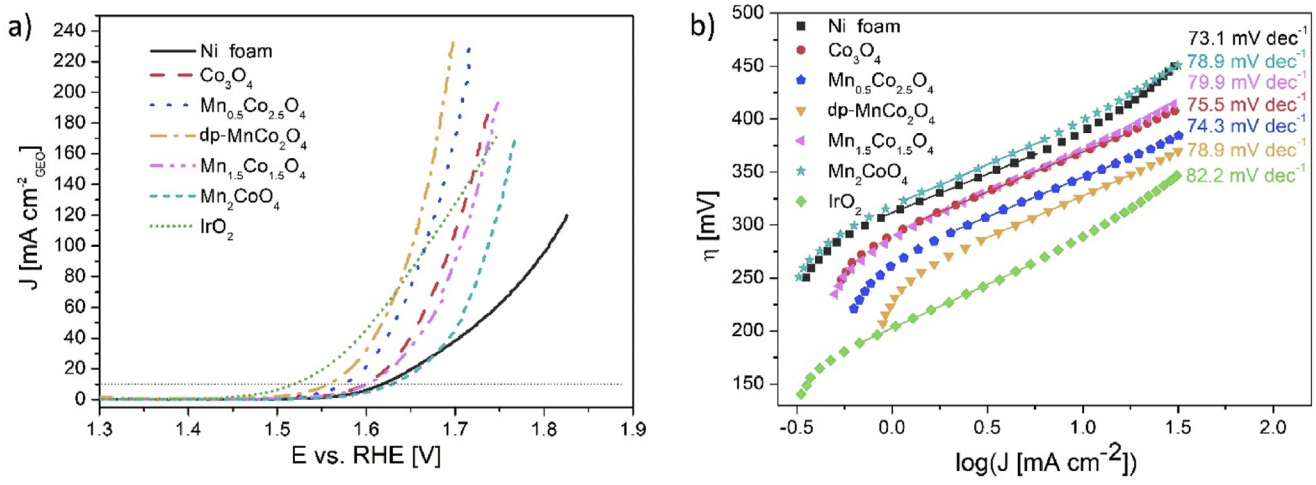

Fig. 5 – (a) Polarisation curves, (b) Tafel plots. All tests were performed in 1.0 M KOH electrolyte.

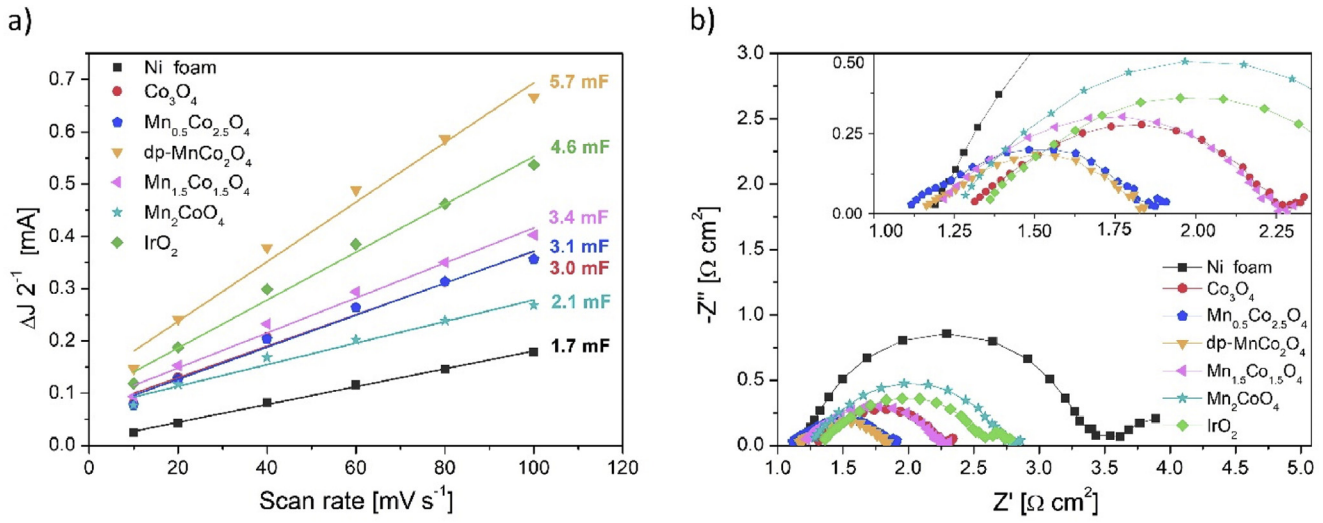

Fig. 6 – (a) Double layer capacitance, (b) EIS spectra at potential of 1.7 V vs. RHE. All tests were performed in 1.0 M KOH electrolyte.

OER mechanism for all of the spinels is similar. The values of the Tafel slopes are characteristic for the limiting process of the electrochemical reaction. The value of 120 mV dec^{-1} represents the limiting process of the first electron transfer step, the slope of 60 mV dec^{-1} is caused by the chemical step, and finally, the value of 40 mV dec^{-1} is representative of the second electron transfer step [52–54]. The values obtained in this work point to a possible mixed mechanism, with a strong influence of the chemical step.

Fig. 6a presents the relationship between the current density and scan rate obtained from cycling voltammetry (CV curves are shown in Fig. S8). Double layer capacitances were used for the calculation of the electrochemically active surface areas (ECSAs) of the catalysts. The collected data was used to calculate C_{dl}, and consecutively ECSA (Table 3). The ECSA increases with the addition of Mn in the $Mn_xCo_{3-x}O_4$ spinel structure for $x \leq 1$, but then the trend reverses. The ECSA demonstrates that the dual-phase $MnCo_2O_4$ has the highest number of active sites, which may be an explanation for its superior OER activity among the prepared spinels. It is important to note that ECSA of $Mn_{0.5}Co_{2.5}O_4$ and Co_3O_4 are almost the same, while the BET specific surface area of $Mn_{0.5}Co_{2.5}O_4$ is 3 times higher than that of Co_3O_4. This indicates that the number of active sites does not correlate with the specific area of the material.

For example, Fe:Ni(OH$_2$)/NF integrated catalysts have an ECSA of 18.04 cm^2 (for 3 × 1 cm^2 nickel foam) [55]. Commercially available spinel nanoparticles of Co_3O_4 and Mn_3O_4 (Sigma Aldrich), have an ECSA of 0.19 and 0.49 m^2 g^{-1}, respectively [56]. For comparison, Zhu et al. reported a $SrNb_{0.1}Co_{0.7}Fe_{0.2}O_{3-\delta}$ perovskite nanorod with a high ECSA of 175 m^2 g^{-1} [57].

Additionally, the EIS was employed in order to study the electrochemical properties of the material in more detail.

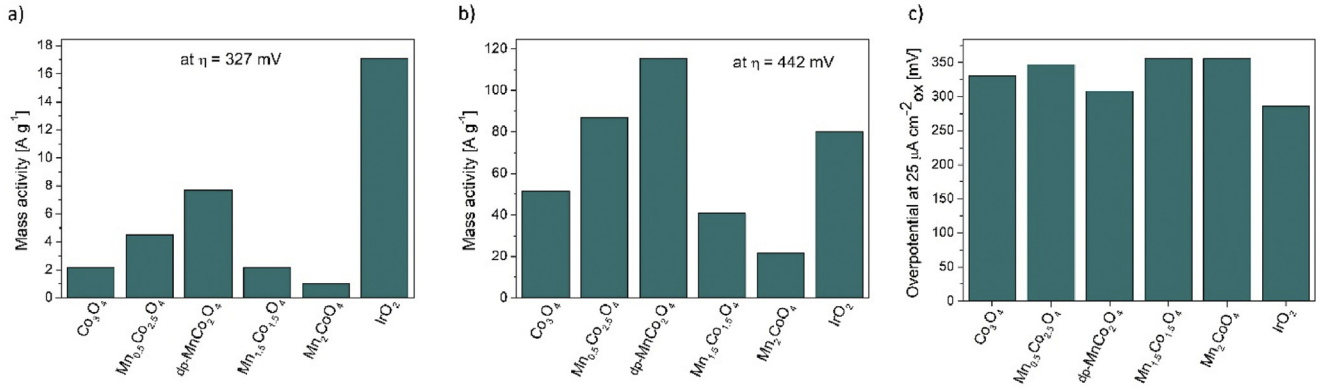

Fig. 7 – Mass and surface specific catalytic activity at η = 327 mV (a) and at η = 442 mV (b) and (c) specific surface activity of catalyst powders.

Nyquist plots obtained by EIS are shown in Fig. 6b. As might be predicted, the dual phase $MnCo_2O_4$ demonstrates the semicircle with the smallest diameter, which indicates the lowest charge transfer resistance among all of the spinels, and results in superior OER activity. The $R_s(CPE\text{-}R_p)$ equivalent circuit was chosen based on the literature reports [3,30,58]. The trend of R_{ct} (Table 3) correlates with the trend of η at 10 mA cm^{-2} i.e. the catalyst with a lower R_{ct} reveals higher OER performance (lower η) due to the faster charge transfer kinetics. The relation suggests that improved charge transfer may be one of the main factors determining OER performance in $Mn_xCo_{3-x}O_4$ spinels.

Based on the above discussion, it seems that the performance of the MnCo2O4 spinel, which is in reality a dual-phase compound consisting of Co_3O_4 and $Mn_{1.15}Co_{1.85}O_4$, is the highest one based on the metrics shown. In the following discussion, other performance metrics are shown, indicating the complex nature of catalyst benchmarking. Namely, the specific weight of the catalyst and its surface area (based on BET) are used.

Fig. 7a and b present the specific mass activities of the catalysts determined at the $\eta = 327$ mV and $\eta = 442$ mV (values of η for dual-phase $MnCo_2O_4$ needed to achieve a current density of 10 mA cm^{-2} and 150 mA cm^{-2}, respectively). In addition, the surface-specific activity was calculated based on the determined BET surface areas and the results are presented in Fig. 7c.

Dual-phase $MnCo_2O_4$ exhibits the highest mass activity among the $Mn_xCo_{3-x}O_4$ spinels and, more importantly, at higher potentials, the dual-phase $MnCo_2O_4$ performance significantly surpasses the performance of IrO_2. The mass activity of the dual-phase $MnCo_2O_4$ at $\eta = 442$ is 115 A g^{-1}, which is about 2.3 and 1.4 times higher than the values for Co_3O_4 and IrO_2, respectively. For instance, Wang et al. reported the mesoporous $MnCo_2O_4$ exhibiting a mass activity of 20.6 mA g^{-1} at 1.6 vs. RHE measured in 0.1 M KOH [59]. On the other hand, Chen et al. have reported mass activities of 1000–9000 A g^{-1} for amorphous BSCF [60]. These very high performances were obtained on 1 nm–20 nm thick films, so their scaling and thus direct comparison to the values with the powder-based catalysts are questionable.

When comparing the surface-specific (BET adjusted) catalyst performance, presented in Fig. 7c, the overpotential values determined at 25 μA cm^{-2} are quite similar, no large differences are noticed. The lowest overpotential values are obtained for the IrO_2 reference catalyst, followed by the $MnCo_2O_4$ catalyst. In this case, it would mean that the performance gain is caused by the extended specific surface area of the powders obtained for Mn-containing compounds. However, this is not entirely true, as the ECSA does not scale linearly with the BET area, and the comparisons are more complex and require further studies.

The catalysts' durability was evaluated by chronopotentiometry tests at a 10 mA cm^{-2} current density performed for 25 h. From the plots presented in Fig. 8 a) it can be seen that all electrodes exhibited an initial large increase of potential in the first 1–2 h. This can be possibly caused by the formation of sticking O_2 bubbles on the electrode surface, and thus decreasing the effective surface coverage. After a stationary state was achieved, the electrode degradation could be discussed.

Up to ~10 h, the spinel materials demonstrated quite stable behaviour. A segment of each plot corresponding to the last 5 h, where the degradation was relatively steady, has been used to estimate the degradation rate. The results plotted in Fig. 8 b) demonstrate a slight loss of performance with a rate of around 0.3–2.5 mV h^{-1}. $MnCo_2O_4$ appears to be the least stable spinel with a performance drop-rate of 2 mV h^{-1}. The reference IrO_2 catalyst shows the lowest initial overpotential and a slow, but visible degradation rate. Notably, the spinels exhibit better stability than the pure Ni foam electrode.

For a broader comparison with the data obtained in this study, results recently reported in the literature for spinels

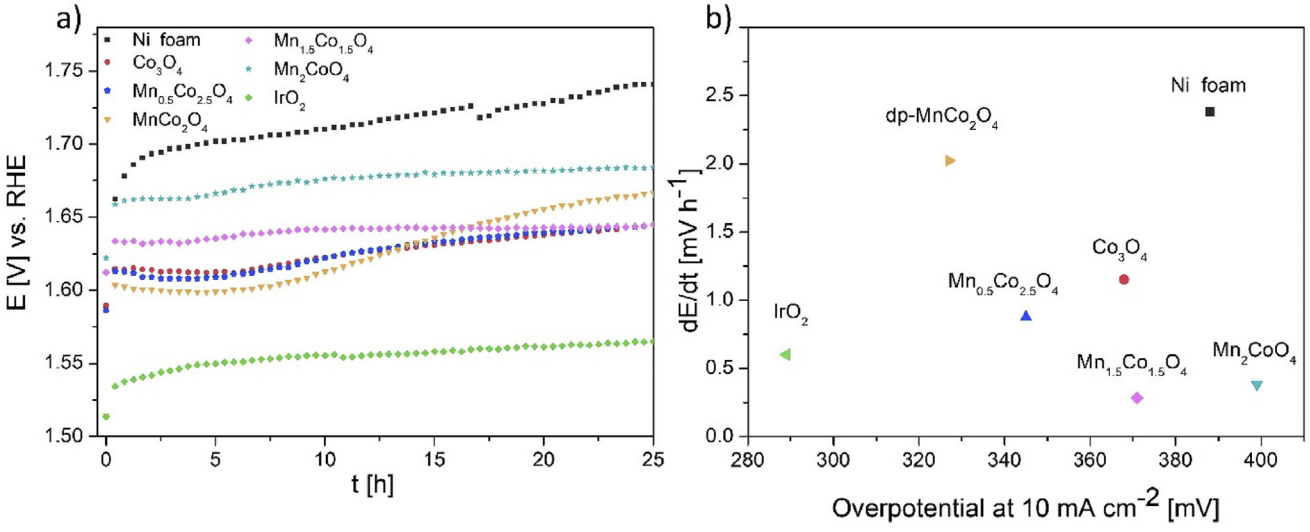

Fig. 8 – a) Potential profiles during chronopotentiometry at 10 mA cm^{-2} current density. b) Degradation rate estimated for the last 5 h of stability test.

Table 4 – Comparison of reported OER electrocatalysts, including Mn-Co spinels.

Catalyst	Electrolyte	Substrate	η at 10 mA cm^{-2} [mV]	Tafel slope [mV dec^{-1}]	Catalyst's loading [mg cm^{-2}]	Ref.
Co_3O_4	1M KOH	**Ni foam**	**368**	**75.5**	**1.30**	**This work**
$MnCo_2O_4$ (Co_3O_4 + $Mn_{1.4}Co_{1.6}O_4$)			**327**	**78.9**		
Co_3O_4 5.9 nm		Ni foam	328	–	1.00	[22]
Flower-like Co_3O_4 on Co foam		Co foam	273	61.8	–	[62]
$MnCo_2O_4$		Glassy Carbon (GC)	560	167	1.48	[64]
Ce-$MnCo_2O_4$-3%			390	120.0	1.48	[64]
$NiCo_2O_4$ nanoflowers with graphene			383	137	–	[63]
MnCo2O4@CoS nanosheets		Ni foam	270 (@20 mA cm-2)	132	–	[61]
rod bundle-like $NiCo_2O_4$			320	59.3	1.0	[65]
Co_3O_4	1M NaOH	Glassy Carbon – Rotating	500	60.9		[56]
$NiFe_2O_4$		Disk electrode (GC-RDE)	510	–		[56]
Mn_3O_4			430	60.9		[56]
$MnCo_2O_4$@NCNTs	0.1M KOH		470	106.0	0.28	[25]
Co_3O_4/$MnCo_2O_4$ nanocomposite			540	–	–	[66]
Co3O4/Ppy/RGO			300	105	~0.1	[67]
$MnCo_2O_4$ microspheres			510	55	0.051	[68]
Mn_2CoO_4 microspheres			600	64	0.051	[68]
mesoporous $MnCo_2O_4$			400	90.0	–	[59]
Mn_2O_3 porous nanoplates		Ni foam	420	81.0	–	[27]

and Mn/Co-based materials are summarised in Table 4. The presented data shows that the $MnCo_2O_4$ on nickel foam synthesised in this work by a EDTA-CA-EG method exhibit improved or comparable electrocatalytic performance to reported spinel-based electrocatalysts. The reached overpotential of 327 mV at 10 mA cm^{-2} can be considered one of the lowest reported for spinels. The lowest overpotential value of 270 (at 20 mA cm^{-2}) for a spinel/sulphide hybrid material in the form of nanosheet was reported by Du et al. [61]. The materials have however a somewhat higher Tafel slope of ~130 mV dec^{-1}. The very low overpotential of this hybrid structure shows the great potential of combining spinels with other materials for improved performance, also supported by other good results [61–63].

Wang et al. have reported a relatively similar well-dispersed nanocomposite of Co_3O_4–$MnCo_2O_4$. In 0.1M KOH it showed a moderate performance of $\eta = 540$ mV at 10 mA cm^{-2} [66]. The catalyst was obtained by separate nucleation and ageing steps (SNAS). Cheng et al. have studied room-temperature synthesised nanocrystalline spinels $M_xMn_{3-x}O_4$ (M = Co, Mg or Zn) for ORR/OER reactions in 0.1M KOH [69]. The authors described, that the low synthesis temperature provided higher electrocatalytic activity and that for OER, the tetragonal phase was more active than the cubic phase. Menezes et al. have compared Mn_2CoO_4 and $MnCo_2O_4$ in the form of microspheres for OER and ORR reactions in 0.1M KOH [68]. Interestingly, the Co-rich cubic compound outperformed the Mn-rich spinel in OER, but the trend was reversed in ORR. In addition, a study by Rios et al. reported that increasing the content of Co in $Mn_xCo_{3-x}O_4$ ($0 \le x \le 1$) improved the OER rate, which was related to the higher Co^{3+} content in the spinel structure [70]. In their case, the best performance was obtained for a pure Co_3O_4 spinel. As reported by Wei et al. [47], tetragonal spinel Mn_2CoO_4 could be expected to exhibit the highest OER catalytic activity, which was not the case in this study.

The differing and sometimes contradicting results obtained by different groups indicate the possible influence of the preparation of the catalyst and measurement procedures on determining the electrocatalytic properties. As pointed out by Wei et al. [47] (for the Mn-Co spinels), and Zhou et al. [71] (in the case of $MnFe_2O_4$), changes in the annealing temperature of the powders can result in oxidation of Mn^{2+} to Mn^{3+} and transfer from tetrahedral to octahedral sites in the lattice. Thus the comparison and discussion are altered by the preparation, thermal history and measurements methodology. More studies are required in order to clarify the observed differences.

The good catalytic properties of the heterogeneous hybrid structure of Co_3O_4 and $Mn_{1.4}Co_{1.6}O_4$ spinels (η of 327 mV at 10 mA cm^{-2}) can result from various factors. Firstly, the addition of Mn causes the powder's grain refinement with a mean particle diameter smaller than 100 nm (determined by BET). Based on TEM, the smaller particles attributable to the mixed Mn-Co phase are smaller than 50 nm. The grain refinement is directly related to the increase of the BET surface area. Esswein et al. determined that the overpotential for water oxidation at a constant current density of 10 mA cm^{-2} decreases by ~50 mV with the increase of catalyst's surface area by an order of magnitude [22]. The ECSA calculated from the electrode's double-layer capacitance is the highest for the electrode coated with dual-phase $MnCo_2O_4$ catalyst (143 cm^2). When recalculated per weight of the catalyst (~1.3 mg), the mass-specific ECSA of the dual-phase $MnCo_2O_4$ is ~11 m^2 g^{-1}. Compared to other reported catalysts, this value seems relatively high.

Additionally, dual-phase $MnCo_2O_4$ exhibits the lowest charge transfer resistance of 0.69 Ω cm^2, which indicates a much higher conductivity compared to other Co-Mn-O catalysts [24]. A combination of a dual-phase structure, relatively high specific surface area and the high conductivity of $MnCo_2O_4$ are the possible explanations of its remarkable activity compared to other stoichiometries [72].

Conclusions

$Mn_xCo_{3-x}O_4$ spinel powders were fabricated via a facile EDTA-CA-EG method. The powders were analysed for their surface area, chemical and phase composition, and their electrocatalytic properties towards oxygen evolution reaction.

The performed electrochemical studies indicated that the low content ($x \leq 1$) of Mn in $Mn_xCo_{3-x}O_4$ enhances its catalytic activity towards OER in an alkaline medium by increasing the number of active sites and lowering the charge transfer resistance. The highest initial performance has been reported for the spinel with the nominal $MnCo_2O_4$ designation, which has been revealed to consist of two cubic phases: Co_3O_4 (~30 vol%) and $Mn_{1.4}Co_{1.6}O_4$ (~70 vol%). This particular material shows very high activity, not explainable by simple additive properties of the two phases. The effects of BET and ECSA surface areas on the OER activity were investigated. Except for $MnCo_2O_4$, all prepared materials revealed relatively good stability with degradation rates similar to IrO_2. Future work will focus on further studies of the effects of the synthesis and microstructure of the spinels on their electrocatalytic activity. Studies of dual-phase materials seem a promising route for further lowering and understanding the complex OER phenomena.

Acknowledgements

The presented research is part of the "Nanocrystalline ceramic materials for efficient electrochemical energy conversion" project, carried out within the First TEAM programme of the Foundation for Polish Science (grant agreement nr. POIR.04.04.00-00-42E9/17-00), co-financed by the European Union under the European Regional Development Fund. Funding from Statutory Funds of WETI PG is also acknowledged.

Appendix A. Supplementary data

Supplementary data to this article can be found online at https://doi.org/10.1016/j.ijhydene.2020.03.188.

REFERENCES

[1] Schmidt O, Gambhir A, Staffell I, Hawkes A, Nelson J, Few S. Future cost and performance of water electrolysis: an expert elicitation study. Int J Hydrogen Energy 2017;42:30470–92. https://doi.org/10.1016/j.ijhydene.2017.10.045.

[2] da Silva FS, de Souza TM. Novel materials for solid oxide fuel cell technologies: a literature review. Int J Hydrogen Energy 2017;42:26020–36. https://doi.org/10.1016/J.IJHYDENE.2017.08.105.

[3] Mitra D, Trinh P, Malkhandi S, Mecklenburg M, Heald SM, Balasubramanian M, et al. An efficient and robust surface-modified iron electrode for oxygen evolution in alkaline water. Electrolysis 2018;165:392–400. https://doi.org/10.1149/2.1371805jes.

[4] Zhu Y, Zhou W, Chen ZG, Chen Y, Su C, Tadé MO, et al. SrNb0.1Co0.7Fe0.2O3-δ perovskite as a next-generation electrocatalyst for oxygen evolution in alkaline solution. Angew Chem Int Ed 2015;54:3897–901. https://doi.org/10.1002/anie.201408998.

[5] Adolphsen JQ, Sudireddy BR, Gil V, Chatzichristodoulou C. Oxygen evolution activity and chemical stability of Ni and Fe based perovskites in alkaline media. J Electrochem Soc 2018;165:F827–35. https://doi.org/10.1149/2.0911810jes.

[6] Zhang J, Cui Y, Jia L, He B, Zhang K, Zhao L. Engineering anion defect in LaFeO2.85Cl0.15 perovskite for boosting oxygen evolution reaction. Int J Hydrogen Energy 2019;44:24077–85. https://doi.org/10.1016/j.ijhydene.2019.07.162.

[7] Xu X, Pan Y, Zhou W, Chen Y, Zhang Z, Shao Z. Toward enhanced oxygen evolution on perovskite oxides synthesized from different approaches: a case study of Ba0.5Sr0.5Co0.8Fe0.2O3−δ. Electrochim Acta 2016;219:553–9. https://doi.org/10.1016/j.electacta.2016.10.031.

[8] Kordek K, Yin H, Rutkowski P, Zhao H. Cobalt-based composite films on electrochemically activated carbon cloth as high performance overall water splitting electrodes. Int J Hydrogen Energy 2019;44:23–33. https://doi.org/10.1016/j.ijhydene.2018.02.095.

[9] Singh RN, Mishra D, Anindita, Sinha ASK, Singh A. Novel electrocatalysts for generating oxygen from alkaline water electrolysis. Electrochem Commun 2007;9:1369–73. https://doi.org/10.1016/j.elecom.2007.01.044.

[10] Huang Y, Yang W, Yu Y, Hao S. Ordered mesoporous spinel CoFe 2 O 4 as efficient electrocatalyst for the oxygen evolution reaction. J Electroanal Chem 2019;840:409–14. https://doi.org/10.1016/j.jelechem.2019.04.010.

[11] Peng S, Gong F, Li L, Yu D, Ji D, Hu Z, et al. Necklace-like multi-shelled hollow spinel oxides with oxygen vacancies for efficient water electrolysis. J Am Chem Soc 2018;140. https://doi.org/10.1021/jacs.8b05134. jacs.8b05134.

[12] Ge X, Liu Y, Goh FWT, Hor TSA, Zong Y, Xiao P, et al. Dual-phase spinel $MnCo_2O_4$ and Spinel $MnCo_2O_4$/nanocarbon hybrids for electrocatalytic oxygen reduction and evolution. ACS Appl Mater Interfaces 2014;6:12684–91. https://doi.org/10.1021/am502675c.

[13] Béjar J, Álvarez-Contreras L, Ledesma-García J, Arjona N, Arriaga LG. Electrocatalytic evaluation of Co3O4 and NiCo2O4 rosettes-like hierarchical spinel as bifunctional materials for oxygen evolution (OER) and reduction (ORR) reactions in alkaline media. J Electroanal Chem 2019;847:113190. https://doi.org/10.1016/j.jelechem.2019.113190.

[14] Sivakumar P, Subramanian P, Maiyalagan T, Gedanken A, Schechter A. Ternary nickel–cobalt–manganese spinel oxide nanoparticles as heterogeneous electrocatalysts for oxygen evolution and oxygen reduction reaction. Mater Chem Phys 2019;229:190–6. https://doi.org/10.1016/j.matchemphys.2019.03.017.

[15] Si S, Hu HS, Liu RJ, Xu ZX, Wang CBin, Feng YY. Co–NiFe layered double hydroxide nanosheets as an efficient electrocatalyst for the electrochemical evolution of oxygen. Int J Hydrogen Energy 2020;45:9368–79. https://doi.org/10.1016/j.ijhydene.2020.01.241.

[16] Liang Z, Zhou P, Wang Z, Wang P, Liu Y, Qin X, et al. Electrodeposition of NiFe layered double hydroxide on Ni3S2 nanosheets for efficient electrocatalytic water oxidation. Int J Hydrogen Energy 2020;45:8659–66. https://doi.org/10.1016/j.ijhydene.2020.01.113.

[17] Yan Q, Kong L, Zhang X, Wei T, Yin J, Cheng K, et al. Vertical Nickel–Iron layered double hydroxide nanosheets grown on hills-like nickel framework for efficient water oxidation and splitting. Int J Hydrogen Energy 2020;45:3986–94. https://doi.org/10.1016/j.ijhydene.2019.12.088.

[18] Cui S, Mtukula AC, Bo X, Guo L. High-efficiency Co6W6C catalyst with three-dimensional ginger-like morphology for promoting the hydrogen and oxygen evolution reactions. Int J Hydrogen Energy 2020;45:6404–15. https://doi.org/10.1016/j.ijhydene.2019.12.160.
[19] Xu S, Wang M, Saranya G, Chen N, Zhang L, He Y, et al. Pressure-driven catalyst synthesis of Co-doped Fe3C@Carbon nano-onions for efficient oxygen evolution reaction. Appl Catal B Environ 2020;268:118385. https://doi.org/10.1016/j.apcatb.2019.118385.
[20] Zhang S, Gao G, Hao J, Wang M, Zhu H, Lu S, et al. Low-electronegativity vanadium substitution in cobalt carbide induced enhanced electron transfer for efficient overall water splitting. ACS Appl Mater Interfaces 2019;11:43261–9. https://doi.org/10.1021/acsami.9b16390.
[21] She S, Zhu Y, Chen Y, Lu Q, Zhou W, Shao Z. Realizing ultrafast oxygen evolution by introducing proton acceptor into perovskites. Adv Energy Mater 2019;1900429:1–6. https://doi.org/10.1002/aenm.201900429.
[22] Esswein AJ, Mcmurdo MJ, Ross PN, Bell AT, Tilley TD. Size-dependent activity of Co3O4 nanoparticle anodes for alkaline water electrolysis. J Phys Chem C 2009;113:15068–72. https://doi.org/10.1021/jp904022e.
[23] Lee E, Jang JH, Kwon YU. Composition effects of spinel MnxCo3-xO4 nanoparticles on their electrocatalytic properties in oxygen reduction reaction in alkaline media. J Power Sources 2015;273:735–41. https://doi.org/10.1016/j.jpowsour.2014.09.156.
[24] Han H, Mhin S. Oxygen evolution reaction of Co-Mn-O electrocatalyst prepared by solution combustion synthesis. https://doi.org/10.3390/catal9060564; 2019.
[25] Zhao T, Gadipelli S, He G, Ward MJ, Do D, Zhang P, et al. Tunable bifunctional activity of $Mn_xCo_{3-x}O_4Na_n$ocrystals decorated on carbon nanotubes for oxygen electrocatalysis. ChemSusChem 2018;11:1295–304. https://doi.org/10.1002/cssc.201800049.
[26] Ishihara T, Yokoe K, Miyano T, Kusaba H. Mesoporous MnCo2O4 spinel oxide for a highly active and stable air electrode for Zn-air rechargeable battery. Electrochim Acta 2019;300:455–60. https://doi.org/10.1016/J.ELECTACTA.2019.01.092.
[27] Sim H, Lee J, Yu T, Lim B. Manganese oxide with different composition and morphology as electrocatalyst for oxygen evolution reaction. Kor J Chem Eng 2018;35:257–62. https://doi.org/10.1007/s11814-017-0247-2.
[28] Sivakumar P, Subramanian P, Maiyalagan T, Gedanken A, Schechter A. Ternary nickel–cobalt–manganese spinel oxide nanoparticles as heterogeneous electrocatalysts for oxygen evolution and oxygen reduction reaction. Mater Chem Phys 2019;229:190–6. https://doi.org/10.1016/j.matchemphys.2019.03.017.
[29] Zhan Y, Xu C, Lu M, Liu Z, Lee JY. Mn and Co co-substituted Fe3O4nanoparticles on nitrogen-doped reduced graphene oxide for oxygen electrocatalysis in alkaline solution. J Mater Chem A 2014;2:16217–23. https://doi.org/10.1039/c4ta03472d.
[30] Wu S, Liu J, Cui B, Li Y, Liu Y, Hu B, et al. Fluorine-doped nickel cobalt oxide spinel as efficiently bifunctional catalyst for overall water splitting. Electrochim Acta 2019;299:231–44. https://doi.org/10.1016/j.electacta.2019.01.012.
[31] Talic B, Hendriksen PV, Wiik K, Lein HL. Thermal expansion and electrical conductivity of Fe and Cu doped MnCo2O4 spinel. Solid State Ionics 2018;326:90–9. https://doi.org/10.1016/j.ssi.2018.09.018.
[32] Kumar M, Awasthi R, Sinha ASK, Singh RN. New ternary Fe, Co, and Mo mixed oxide electrocatalysts for oxygen evolution. Int J Hydrogen Energy 2011;36:8831–8. https://doi.org/10.1016/j.ijhydene.2011.04.071.
[33] Singh NK, Yadav R, Yadav MK. Electrocatalytic activity of NixFe3-xO4 ($0 \leq x \leq 1.5$) obtained by natural egg ovalbumin for alkaline water electrolysis. J New Mater Electrochem Syst 2016;19:209–15.
[34] Maček J, Novosel B, Zupan K, Razpotnik T, Francetič V, Marinšek M. A polymer complex solution process for the synthesis and characterization of Ni–YSZ cermet material. Ceram Int 2007;34:1741–6. https://doi.org/10.1016/j.ceramint.2007.05.006.
[35] Wang HY, Hung SF, Chen HY, Chan TS, Chen HM, Liu B. In operando identification of geometrical-site-dependent water oxidation activity of spinel Co3O4. J Am Chem Soc 2016;138:36–9. https://doi.org/10.1021/jacs.5b10525.
[36] Rodriguez-Carvajal J. Recent advances in magnetic structure determination by neutron powder diffraction. Phys B 1993:55–69. https://doi.org/10.1016/0921-4526(93)90108-I.
[37] Bordeneuve H, Rousset A, Tenailleau C, Guillemet-Fritsch S. Cation distribution in manganese cobaltite spinels Co3-xMnxO4($0 \leq x \leq 1$) determined by thermal analysis. J Therm Anal Calorim 2010;101:137–42. https://doi.org/10.1007/s10973-009-0557-7.
[38] Habjanic J, Juric M, Popovic J, Molcanov K, Pajic D. A 3D oxalate-based network as a precursor for the CoMn2O4 spinel: synthesis and structural and magnetic studies. Inorg Chem 2014:9633–43. https://doi.org/10.1063/1.5087986.
[39] Andersson JO, Helander T, Höglund L, Shi P, Sundman B. Thermo-Calc & DICTRA, computational tools for materials science. Calphad Comput Coupling Phase Diagrams Thermochem 2002;26:273–312. https://doi.org/10.1016/S0364-5916(02)00037-8.
[40] Weiland R. Untersuchungen zur Thermodynamik oxidischer Lösungsphasen im System Co-Fe-Mn-O. Arbeit; 2002.
[41] Shukla S, Bhattacharjee S, Weber AZ, Secanell M. Experimental and theoretical analysis of ink dispersion stability for polymer electrolyte fuel cell applications. J Electrochem Soc 2017;164:F600–9. https://doi.org/10.1149/2.0961706jes.
[42] Li G, Yang D, Chuang P-Y. Defining Nafion ionomer roles for enhancing alkaline oxygen evolution electrocatalysis. ACS Catal 2018. https://doi.org/10.1021/acscatal.8b02217. acscatal.8b02217.
[43] Stelmachowski P, Monteverde Videla AHA, Ciura K, Specchia S. Oxygen evolution catalysis in alkaline conditions over hard templated nickel-cobalt based spinel oxides. Int J Hydrogen Energy 2017;42:27910–8. https://doi.org/10.1016/j.ijhydene.2017.06.034.
[44] McCrory CCL, Jung S, Peters JC, Jaramillo TF. Benchmarking heterogeneous electrocatalysts for the oxygen evolution reaction. J Am Chem Soc 2013;135:16977–87. https://doi.org/10.1021/ja407115p.
[45] Zhang S, Sun X, Zheng Z, Zhang L. Nanoscale center-hollowed hexagon MnCo2O4 spinel catalyzed aerobic oxidation of 5-hydroxymethylfurfural to 2,5-furandicarboxylic acid. Catal Commun 2018;113:19–22. https://doi.org/10.1016/j.catcom.2018.05.004.
[46] Lavela P, Tirado JL, Vidal-Abarca C. Sol–gel preparation of cobalt manganese mixed oxides for their use as electrode materials in lithium cells. Electrochim Acta 2007;52:7986–95. https://doi.org/10.1016/j.electacta.2007.06.066.
[47] Wei C, Feng Z, Scherer GG, Barber J, Shao-Horn Y, Xu ZJ. Cations in octahedral sites: a descriptor for oxygen electrocatalysis on transition-metal spinels. Adv Mater 2017;29. https://doi.org/10.1002/adma.201606800.
[48] Zhao Q, Yan Z, Chen C, Chen J. Spinels: controlled preparation, oxygen reduction/evolution reaction application, and beyond. Chem Rev 2017;117:10121–211. https://doi.org/10.1021/acs.chemrev.7b00051.

[49] Kruk A, Stygar M, Brylewski T. Mn-Co spinel protective-conductive coating on AL453 ferritic stainless steel for IT-SOFC interconnect applications. J Solid State Electrochem 2013;17:993–1003. https://doi.org/10.1007/s10008-012-1952-8.
[50] Talic B, Hendriksen PV, Wiik K, Lein HL. Thermal expansion and electrical conductivity of Fe and Cu doped MnCo2O4spinel. Solid State Ionics 2018;326:90–9. https://doi.org/10.1016/j.ssi.2018.09.018.
[51] Bobruk M, Brylewska K, Durczak K, Wojciechowski K, Adamczyk A, Brylewski T. Synthesis of manganese-cobalt spinel via wet chemistry methods and its properties. Ceram Int 2017;43:15597–609. https://doi.org/10.1016/j.ceramint.2017.08.116.
[52] Anantharaj S, Karthick K, Kundu S. Evolution of layered double hydroxides (LDH) as high performance water oxidation electrocatalysts: a review with insights on structure, activity and mechanism. Mater Today Energy 2017;6:1–26. https://doi.org/10.1016/j.mtener.2017.07.016.
[53] Browne MP, Nolan H, Duesberg GS, Colavita PE, Lyons MEG. Low-overpotential high-activity mixed manganese and ruthenium oxide electrocatalysts for oxygen evolution reaction in alkaline media. ACS Catal 2016;6:2408–15. https://doi.org/10.1021/acscatal.5b02069.
[54] Doyle RL, Godwin IJ, Brandon MP, Lyons MEG. Redox and electrochemical water splitting catalytic properties of hydrated metal oxide modified electrodes. Phys Chem Chem Phys 2013;15:13737–83. https://doi.org/10.1039/c3cp51213d.
[55] Zhang W, Qi J, Liu K, Cao R. A nickel-based integrated electrode from an autologous growth strategy for highly efficient water oxidation. Adv Energy Mater 2016;6:1502489. https://doi.org/10.1002/aenm.201502489.
[56] Jung S, McCrory CCL, Ferrer IM, Peters JC, Jaramillo TF. Benchmarking nanoparticulate metal oxide electrocatalysts for the alkaline water oxidation reaction. J Mater Chem A 2016;4:3068–76. https://doi.org/10.1039/c5ta07586f.
[57] Zhu Y, Zhou W, Zhong Y, Bu Y, Chen X, Zhong Q, et al. A perovskite nanorod as bifunctional electrocatalyst for overall water splitting. Adv Energy Mater 2017;7:10–7. https://doi.org/10.1002/aenm.201602122.
[58] Béjar J, Álvarez-Contreras L, Ledesma-García J, Arjona N, Arriaga LG. Electrocatalytic evaluation of Co3O4 and NiCo2O4 rosettes-like hierarchical spinel as bifunctional materials for oxygen evolution (OER) and reduction (ORR) reactions in alkaline media. J Electroanal Chem 2019. https://doi.org/10.1016/j.jelechem.2019.113190.
[59] Wang W, Kuai L, Cao W, Huttula M, Ollikkala S, Ahopelto T, et al. Mass-production of mesoporous MnCo2O4 spinels with manganese(IV)- and Cobalt(II)-rich surfaces for superior bifunctional oxygen electrocatalysis. Angew Chem Int Ed 2017;56:14977–81. https://doi.org/10.1002/anie.201708765.
[60] Chen G, Zhou W, Guan D, Sunarso J, Zhu Y, Hu X, et al. Two orders of magnitude enhancement in oxygen evolution reactivity on amorphous Ba0.5Sr0.5Co0.8Fe0.2O3–d nanofilms with tunable oxidation state. Sci Adv 2017;3:1–9. https://doi.org/10.1126/sciadv.1603206.
[61] Du X, Su H, Zhang X. 3D MnCo2O4@CoS nanoarrays with different morphologies as an electrocatalyst for oxygen evolution reaction. Int J Hydrogen Energy 2019;44:21637–50. https://doi.org/10.1016/j.ijhydene.2019.06.086.
[62] Zhang L, Liang Q, Yang P, Huang Y, Chen W, Deng X, et al. Flower-like Co3O4 microstrips embedded in Co foam as a binder-free electrocatalyst for oxygen evolution reaction. Int J Hydrogen Energy 2019;44:24209–17. https://doi.org/10.1016/j.ijhydene.2019.07.146.
[63] Li Z, Li B, Chen J, Pang Q, Shen P. Spinel NiCo2O4 3-D nanoflowers supported on graphene nanosheets as efficient electrocatalyst for oxygen evolution reaction. Int J Hydrogen Energy 2019;44:16120–31. https://doi.org/10.1016/j.ijhydene.2019.04.219.
[64] Huang X, Zheng H, Lu G, Wang P, Xing L, Wang J, et al. Enhanced water splitting electrocatalysis over $MnCo_2O_4$ via introduction of suitable Ce content. ACS Sustainable Chem Eng 2018. https://doi.org/10.1021/acssuschemeng.8b04814. acssuschemeng.8b04814.
[65] Li Z, Gu A, He X, Lv H, Wang L, Lou Z, et al. Rod bundle-like nickel cobaltate derived from bimetal-organic coordination complex as robust electrocatalyst for oxygen evolution reaction. Solid State Ionics 2019;331:37–42. https://doi.org/10.1016/j.ssi.2018.12.022.
[66] Wang D, Chen X, Evans DG, Yang W. Well-dispersed Co3O4/Co2MnO4 nanocomposites as a synergistic bifunctional catalyst for oxygen reduction and oxygen evolution reactions. Nanoscale 2013;5:5312. https://doi.org/10.1039/c3nr00444a.
[67] Jayaseelan SS, Bhuvanendran N, Xu Q, Su H. Co3O4 nanoparticles decorated Polypyrrole/carbon nanocomposite as efficient bi-functional electrocatalyst for electrochemical water splitting. Int J Hydrogen Energy 2020;45:4587–95. https://doi.org/10.1016/j.ijhydene.2019.12.085.
[68] Menezes PW, Indra A, Sahraie NR, Bergmann A, Strasser P, Driess M. Cobalt-manganese-based spinels as multifunctional materials that unify catalytic water oxidation and oxygen reduction reactions. ChemSusChem 2015;8:164–7. https://doi.org/10.1002/cssc.201402699.
[69] Cheng F, Shen J, Peng B, Pan Y, Tao Z, Chen J. Rapid room-temperature synthesis of nanocrystalline spinels as oxygen reduction and evolution electrocatalysts. Nat Chem 2011;3:79–84. https://doi.org/10.1038/nchem.931.
[70] Rios E, Chartier P, Gautier JL. Oxygen evolution electrocatalysis in alkaline medium at thin MnxCo3-xO4 ($0 \leq x \leq 1$) spinel films on glass/SnO2 : F prepared by spray pyrolysis. Solid State Sci 1999;1:267–77. https://doi.org/10.1016/S1293-2558(00)80081-3.
[71] Zhou Y, Du Y, Xi S, Xu ZJ. Spinel manganese ferrites for oxygen electrocatalysis: effect of Mn valency and occupation site. Electrocatalysis 2018;9:287–92. https://doi.org/10.1007/s12678-017-0429-z.
[72] Ma TY, Dai S, Jaroniec M, Qiao SZ. Synthesis of highly active and stable spinel-type oxygen evolution electrocatalysts by a rapid inorganic self-templating method. Chem - A Eur J 2014;20:12669–76. https://doi.org/10.1002/chem.201403946.